

THESIS FOR THE DEGREE OF LICENTIATE OF ENGINEERING

Stacking of interferometric data at sub-millimeter and radio wavelengths

LUKAS LINDROOS



CHALMERS

Department of Earth and Space Sciences
CHALMERS UNIVERSITY OF TECHNOLOGY
Göteborg, Sweden 2014

Stacking of interferometric data at sub-millimeter and radio wavelengths
LUKAS LINDROOS

© Lukas Lindroos, 2014

Radio Astronomy & Astrophysics Group
Department of Earth and Space Sciences
Chalmers University of Technology
SE-412 96 Göteborg, Sweden
Phone: +46 (0)31-772 1000

Contact information:

Lukas Lindroos
Onsala Space Observatory
Chalmers University of Technology
SE-439 92 Onsala, Sweden

Phone: +46 (0)31-772 5543
Email: lukas.lindroos@chalmers.se

Printed by Chalmers Reproservice
Chalmers University of Technology
Göteborg, Sweden 2014

Stacking of interferometric data at sub-millimeter and radio wavelengths

Lukas Lindroos

Department of Earth and Space Sciences
Chalmers University of Technology

Abstract

Understanding the processes of galaxy evolution require observational constraints on the physical properties of galaxies at different times in the history of the Universe. Large and deep surveys at visible and near-infrared wavelengths have, during the past decade, been used to produce extensive catalogues of high-redshift galaxies, spanning a large range of the history of the Universe. However, to properly understand the properties of these galaxies, and the processes they are going through, we need study them across the full electromagnetic spectrum. Observing the galaxies at mm and radio wavelengths add additional probes of the star formation, and allow us to further constrain their properties. Current radio/mm/submm high-redshift galaxy surveys, however, primarily probe luminous starbursts and AGN. A way to probe the radio and mm emission from less luminous galaxies is stacking. Stacking is a statistical approach to measure the average flux for known objects that are too faint to be detected individually at the target wavelength.

This thesis investigates stacking of interferometric data. Typically, stacking at different wavelengths ranges is done using deep imaging surveys observed with a single telescope. However, interferometry is not a direct imaging method, and this presents a number of challenges to stacking. We present a new stacking algorithm that works directly on visibilities, which we refer to as uv-stacking. We compare this algorithm to an image-stacking algorithm, i.e., an algorithm that stacks the sources directly in the imaged data. The uv-stacking algorithm is found to yield more robust results than the image-stacking algorithm. In the case of JVLA surveys, uv-stacking results in a post-stacking signal-to-noise ratio up to 40% higher compared to image-stacking. Furthermore, it is possible to use the algorithms to estimate an average size of the stacked source population. Stacking marginally extended sources of $1''.5$ for JVLA, we find that the typical uncertainties of sizes measured with image-stacking are more than twice that of uv-stacking.

The stacking techniques are applied to colour-selected, high-redshift galaxies in the 344 GHz continuum survey ALESS (the ALMA survey of sources detected in the LABOCA Extended Chandra deep field south (ECDFS) Submillimetre Survey) and the VLA 1.4 GHz continuum of the ECDFS. Using the uv-stacking algorithm, the average sizes of the galaxies are measured to be around $1''$, which correspond to a physical size of ~ 8 kpc at $z \sim 2$. Within the uncertainties, the stacked average sizes are consistent with sizes measured at visible and near-infrared wavelengths.

While the uv-stacking algorithm is designed primarily around stacking high-redshift

galaxies in ALMA and VLA, it can easily be extended to work for other interferometric telescopes and use cases. In particular, the uv-stacking algorithm has been shown to alleviate the effects of high dynamic range, which will be important for future telescopes such as the SKA.

Keywords: techniques: interferometric – methods: data analysis – galaxies: high-redshift – radio continuum: galaxies – sub-millimetre: galaxies

Research contributions

This thesis is based on work described in the following papers.

- I L. Lindroos, K. K. Knudsen, W. Vlemmings, J. Conway, & I. Martí-Vidal:
Stacking of large interferometric data sets in the image- and uv-domain – a comparative study
- II R. Decarli, I. Smail, F. Walter, A. M. Swinbank, T. R. Greve, J. A. Hodge, R. Ivison, A. Karim, K. K. Knudsen, L. Lindroos, H. W. Rix, E. Schinnerer, J. M. Simpson, P. van der Werf, & A. Weiß:
An ALMA Survey of Sub-millimeter Galaxies in the Extended Chandra Deep Field South: Sub-millimeter Properties of Color-selected Galaxies

Acknowledgements

First, I would like to thank my Kirsten Kraiberg Knudsen. Without her persistent support this work would not have been possible. Thank you!

I would also like to thank supervisor John Conway, together with Wouter Vlemmings and Ivan Martí-Vidal. You have provided invaluable feedback to my work and have been patient with my many questions. And a special thank you to John Black, your many good comments greatly improved the quality of this thesis.

Thank you all my colleagues to all my colleagues at Onsala and Chalmers, for making this a great place to work, as well as for sharing your knowledge to broaden mine.

Lukas

Contents

Abstract	i
Research contributions	iii
Acknowledgements	v
1 Introduction	1
1.1 Galaxies, colour selection criteria	2
1.1.1 Lyman-break galaxies	2
1.1.2 BzK galaxies	4
1.1.3 Distant red galaxies	5
1.1.4 Extremely red objects	5
1.2 Observing at radio and sub-mm wavelengths	6
1.2.1 Sub-mm dust continuum as tracer of star-formation	6
1.2.2 Radio continuum as tracer of star-formation	6
1.2.3 Calculating the star formation rates	7
1.3 Typical brightness of high redshift galaxies	8
2 Stacking	11
2.1 Interferometry	13
2.1.1 uv -coverage	14
2.1.2 Imaging	14
2.1.3 Wide field effects	16
2.1.4 Translation and stacking	16
2.2 Simulation details, method of generation of sources.	17
2.2.1 Lyman-break galaxies	18
2.2.2 Radio flux distribution	19
2.2.3 Sub-mm flux distribution	19
2.3 Computational considerations	20
3 Stacking of colour-selected galaxies with ALMA and VLA	23
3.1 Removing bright sources	24
3.2 Recalculating weights	24

3.3	Results	24
3.4	Sizes of stacked sources	27
3.4.1	Measurements	27
3.4.2	Interpretation	27
4	Outlook	31
	References	33
	Paper I	35
	Paper II	36

Introduction

Looking back at the universe in time, at the cosmic microwave background radiation, we can observe at early time the universe was mostly homogeneous. However, looking out at the current day universe the picture is very different. Almost all light comes from galaxies, dense clumps of stars and gas. The field of galaxy formation and evolution concerns understanding this transformation of the universe. From the first galaxy seeds all the way to present-day galaxies.

The most distant galaxies observed have a redshift $z \sim 7.5$ (Finkelstein et al. 2013), with tentative detection of galaxies with redshifts as high as 10 (Ellis et al. 2013; Oesch et al. 2013). Observations of galaxies at different redshifts indicate that in total relatively few stars are formed at these high redshifts. Studying galaxies closer than $z \sim 7$ the star formation rate in a given volume of space (star formation density) quickly picks up and reaches a peak between redshift 2 and 3 (Bouwens et al. 2011) or 2-3 billion years after the Big Bang. After the peak, the star formation density decreases, and appears to be still dropping today.

The general frame-work of galaxy formation and evolution is set by our cosmological model. The currently accepted cosmological model (called Λ CDM), dictates that the universe at early times was dominated by cold dark matter, a matter consisting of heavy particles that interact only through gravitation. Through the process of inflation, where the universe rapidly increased its size, small quantum perturbations in the dark matter form larger over densities, which grow into dark matter halos. In these dark matter halos baryonic gas is gathered. This gas cools through radiation and collapses to form regions dense enough to start forming stars. These collection of gas and stars grow, either through merging with other galaxies or by accreting loose baryonic gas, to form the galaxy zoo of today.

While this model describes the general trends well, there are many details in this picture that are still uncertain. Many unanswered questions remain, such

as: What is the role of mergers versus the role of secular evolution, i.e. galaxies forming stars at a steady rate, being fed by streams of gas from the intergalactic medium? Is star formation constant or does it happen in bursts? What internal mechanisms regulate star formation in galaxies?

To answer these questions we need further observations, at many different wavelengths. The work presented in this thesis revolves around two methods to estimate the star formation properties of high redshift galaxies, and how we can use interferometric telescopes to further these studies. In particular, I will discuss the technique of stacking, which can be used to study populations of faint galaxies. Firstly, in section 1.1 we discuss techniques that can be used to identify high redshift galaxies. In section 1.2 we expand on how star formation rate of high redshift galaxies can be measured by studying their sub-mm and radio continuum emission.

1.1 Galaxies, colour selection criteria

The first step in studies of galaxies is to identify galaxies. A star-forming galaxy emits light according to the spectral energy distribution (SED) in figure 1.1. This SED can be divided roughly into two bumps, one bump at shorter wavelength, in rest frame peaking in visible light, and is dominated by light coming directly from the stars. The other bump, at longer wavelengths dominated by thermal emission from interstellar dust heated by the stars. These two bumps are roughly equal in total energy emitted. Light is also emitted at shorter and longer wavelengths, but this is a small contribution to the energy budget compared to the visible and infrared features.

Selection criteria can be defined across the whole electromagnetic spectrum. At different wavelength ranges different physical processes dominate and this determines the types of galaxies selected by the criteria. Searching for high-redshift galaxies is typically done using imaging photometry. This allows to maximise the amount of sky covered for a given depth. In most cases broadband filters are used and the selection criteria are defined in terms of flux ratios of the different filters. For each filter sources are located and then cross-identified between the different bands. For each source, the total flux in each filter is determined. Based on these fluxes the type of each source is identified. Some of the most commonly used galaxy identification method are the Lyman break and Balmer/4000 Å break criteria.

1.1.1 Lyman-break galaxies

Photons with energies that approach the ionisation potential for neutral hydrogen have difficulties escaping a galaxy (Leitherer & Heckman 1995). This leads to the SED dropping at this wavelength, the so-called *Lyman break*, which falls

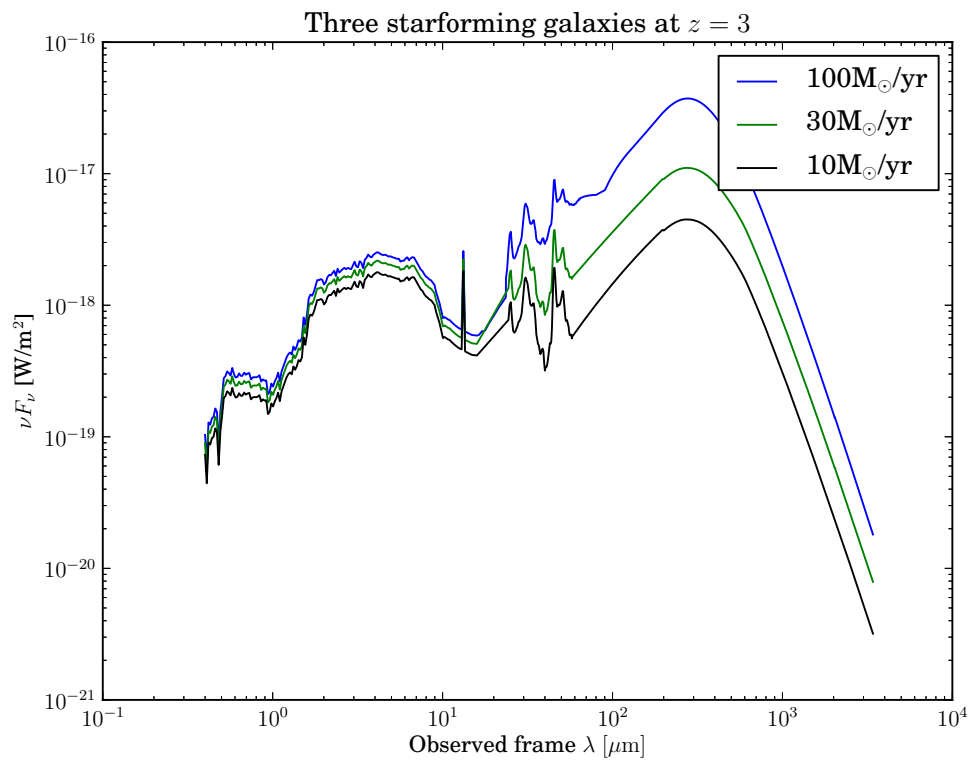


Figure 1.1: Typical spectral energy distribution (SED), from rest frame ultraviolet to far-infrared, for star-forming galaxies at redshift $z = 3$ (Chary & Elbaz 2001).

at 912 Å in the galaxy's rest frame. This can be used to identify galaxies solely based on photometry. For galaxies around $z \sim 3$ we can use the photometric bands U , G and R (365, 600 and 660 nm). In this case the Lyman break falls between the U and G band, leading to low flux in U , and approximately flat spectrum between G and R . The original criteria used by Steidel et al. (1995) were

$$\frac{F_G}{F_U} > \left(\frac{F_R}{F_G} \right)^4 \quad (1.1)$$

and

$$\frac{F_R}{F_G} > 3.02 \quad (1.2)$$

where F_G , F_R and F_U are the flux density in the U , G and R band. Typically the Lyman-break criteria are expressed in term of magnitude differences instead of flux ratios. In AB magnitudes these criteria become $U - G > 4(G - R)$ and $G - R > 2.76$. A galaxy that satisfies the Lyman-break criteria is referred to as a *Lyman-break galaxy* (LBG).

The exact bands used are often shifted around a little depending on the data available in different surveys. This will change around the exact criteria but the general principle is the same.

Equivalent criteria can be used to detect galaxies at higher redshift by shifting all used bands to longer wavelengths (Steidel et al. 1999). This has been used to search for galaxies as far out as $z \approx 10$, e.g., Bouwens et al. (2011).

1.1.2 BzK galaxies

Dusty galaxies can be difficult to detect with the Lyman-break criteria. The dust will absorb ultraviolet-light from stars and lead to galaxies that are faint around the Lyman break. This leads to galaxies with no apparent Lyman break.

Over a range of stellar types, the limit of the hydrogen Balmer series appears as a nearly discontinuous change in flux near 4000 Å, referred to as the *Balmer/4000 Å break*. The BzK selection criteria use this break to identify galaxies (Daddi et al. 2004). The BzK criteria are named after the three photometric band used in the selection: B , z , and K . These criteria selects to galaxies around $z \sim 2$. The 4000 Å break is present for galaxies with little star formation as well as for galaxies with high star formation. However, by tweaking the selection criteria, we determine which we target. This divides the BzK into two sub-populations, the active (sBzK) and the passive (pBzK) population, with the active typically having order of magnitude higher star formation rates.

The sBzK criteria are

$$\frac{F_K}{F_z} > 1.2 \frac{F_z}{F_B} \quad (1.3)$$

or $(z - K) - (B - z) > -0.2$ in AB magnitudes and the pBzK criteria are

$$\frac{F_K}{F_z} < 1.2 \frac{F_z}{F_B} \quad (1.4)$$

combined with

$$\frac{F_K}{F_z} > 10 \quad (1.5)$$

or $(z - K) - (B - z) < -0.2 \cap (z - K) > 2.5$ in AB magnitudes.

1.1.3 Distant red galaxies

Another way to look for high-redshift galaxies is to look for particularly red objects. This can be done by using the infrared bands of J and K at $1.2\mu\text{m}$ and $2.2\mu\text{m}$. The idea being to look for the Balmer/4000Å break at $z \sim 2$ to 4. The distant red galaxy (DRG) criteria are

$$\frac{F_K}{F_J} > 3.37 \quad (1.6)$$

where F_K and F_J are the flux densities in K and J band, Franx et al. (2003) ($J_{\text{AB}} - K_{\text{AB}} > 1.32$ in AB magnitudes). This has been found to select massive galaxies around redshift 2. The selection of red galaxies may include those with old stellar populations that are relatively deficient in blue light, as well as galaxies with a large content of dust that obscures the light from young stars.

1.1.4 Extremely red objects

Another selection criterion for red, high redshift galaxies is the one that selects the so-called extremely red objects (EROs). Elston et al. (1988) showed that it was possible to find high redshift galaxies with

$$\frac{F_K}{F_R} > 21.88 \quad (1.7)$$

or $R - K > 3.7$ in AB magnitudes.

1.2 Observing at radio and sub-mm wavelengths

While most galaxies can be found using surveys in visible light and near-infrared, there is much more information to be obtained by observing the galaxies more wavelength bands. Moving from the near-infrared into the mid- and far-infrared, we can observe the dust emission from galaxies. The dust is primarily heated by hot young stars and as such this emission can be used to trace ongoing star formation.

However, Earth's atmosphere is opaque over a large part of the infrared range, and consequently it is very difficult to observe galaxies near the peak of the far-infrared dust SED. It is required to go into space, as was done with e.g., Herschel Space Observatory. There is a challenge with telescopes in space, the limited aperture. With the small aperture size comes a low angular resolution at far-infrared wavelengths, for Herschel Space observatory this limits the angular resolution to $20''$ at $300\mu\text{m}$. This makes it challenging to study faint galaxies, as they will be blended with emission from other sources within the large beam.

1.2.1 Sub-mm dust continuum as tracer of star-formation

An option to study the dust emission is to go to mm wavelengths. When the wavelength approaches a little less than one mm, the atmosphere is transparent enough to observe from the top of mountains, at sites such as Chajnantor plateau in Chile or Mauna Kea in Hawai'i. At these wavelengths we are able to observe the Rayleigh-Jeans tail of the dust emission. By combining a large number of dishes into an interferometer we can also achieve good resolution at these wavelengths. The most sensitive interferometer at mm wavelengths is the Atacama Large Millimeter/sub-millimeter Array (ALMA).

An advantage with observing at the Rayleigh-Jeans tail is that we are not very sensitive to redshift. The higher the redshift of the target galaxy, the closer to the dust emission peak we will observe it. This results in the so called *negative K-correction*, where, for a given far-infrared luminosity, the observed flux is almost constant for redshift $z = 1 - 8$.

1.2.2 Radio continuum as tracer of star-formation

Another method to measure the star formation of galaxies is to go to even longer wavelengths. Stars of mass greater than around eight solar masses will go supernovae after a few tens of million years. Such supernovae will eject large number of relativistic electrons that will lead to synchrotron radiation. This means that a galaxy with recent star formation will emit light at wavelengths around a few tens of cm, this emission has been shown to be an effective mea-

sure of star formation (Condon 1992). Unlike measures of star formation using ultraviolet or infrared radiation, radio continuum is independent of dust extinction. However, if the galaxy contains an active galactic nuclei (AGN), this may also emit light at similar wavelengths. As such it provides a valuable independent measure of the star-formation rate of galaxies with low AGN activity. There are several interferometers operating at radio wavelengths, which can be used to measure emission few tens of cm, the most sensitive is the Karl G. Jansky Very Large Array (JVLA).

1.2.3 Calculating the star formation rates

The dust emission can often be described approximately as a modified black body (e.g. Beelen et al. 2006)

$$F_\nu \propto \nu^\beta B_\nu(T_{\text{dust}}) \quad (1.8)$$

where $B_\nu(T_{\text{dust}})$ is the Planck function and T_{dust} is the dust temperature. From this we calculate the IR luminosity of the galaxy (L_{IR}) as the integral of the total modified black body emission from 8 μm to 1000 μm .

To calculate L_{IR} from our data we need to account for the redshift of our target source. If we measure a source $z = 2$ using ALMA, with the band 7 receiver ($\nu \sim 345$ GHz), we are in fact sampling the dust SED at $(z + 1)\nu \approx 1.035$ THz. We also must consider that the ALMA bandwidth will cover a larger part of the SED. To correct for this the measured flux must be divided by $(z + 1)$.

Finally, we need to go from flux density to total luminosity. This involves using a cosmological model, in this work we assume a flat universe with $\Omega_M = 0.315$ and $H_0 = 67.3$ km s⁻¹ Mpc⁻¹ (Planck Collaboration et al. 2013). Using this we can calculate the luminosity distance $D_L(z)$.

Combing all we arrive at

$$L_{\text{IR}} = 4\pi D_L^2(z) \int_{c/1000\mu\text{m}}^{c/8\mu\text{m}} \nu^\beta B_\nu(T_{\text{dust}}) d\nu \frac{F_{\nu_{\text{obs}}}}{((z + 1)\nu_{\text{obs}})^\beta B_{(z+1)\nu_{\text{obs}}}(T_{\text{dust}})} \quad (1.9)$$

where ν_{obs} is the frequency of the observations. We then convert this into a star formation rate

$$\frac{\text{SFR}_{\text{FIR}}}{M_\odot \text{ yr}^{-1}} = 1.3 \cdot 10^{-10} \frac{L_{\text{IR}}}{L_\odot}. \quad (1.10)$$

This is the same conversion used in paper II and is based on the the work by Kennicutt (1998) adapted with a Chabrier (2003) initial mass function. The initial mass function (IMF) describes the mass distribution of newly formed stars. The shape of the IMF is important for star formation measures, as it determines the number of massive stars that are formed for a given star formation rate.

For radio continuum we convert the flux into a luminosity in a similar manner assuming that the SED in radio follows a power law

$$F_\nu \propto \nu^\alpha. \quad (1.11)$$

This results in a radio luminosity of

$$L_\nu = \frac{4\pi D_L^2(z)}{(1+z)^{1+\alpha}} F_\nu \quad (1.12)$$

where F_ν is the measured flux at observer-frame frequency ν and L_ν is corrected to be the luminosity at rest-frame frequency ν . Using the model from Condon (1992) we convert this into a star formation rate

$$\frac{\text{SFR}_{1.4\text{GHz}}}{M_\odot \text{yr}^{-1}} = 2.47 \cdot 10^{-22} \frac{L_{1.4\text{GHz}}}{\text{W/Hz}}. \quad (1.13)$$

The spectral index α has been found to be around -0.8 and we use this value.

1.3 Typical brightness of high redshift galaxies

Figure 1.2 shows a few examples of spectral energy distributions (SED) for high-redshift, star-forming galaxies. For comparison we include the sensitivity of ALMA and JVLA, currently the most sensitive interferometers at their respective wavelengths. At $z = 3$, it is difficult to observe galaxies with star formation rates below a few tens of solar masses per year. A technique that can be used to be push past this is *stacking*. Stacking is a statistical method that can be used for populations of galaxies to obtain their average properties.

In this thesis we will discuss stacking in the context of interferometric data. Chapter 2 discusses paper I, which studies two methods to stack interferometric data. In chapter 3 we apply our stacking from paper I to the ALESS data set, to study the properties of several populations of galaxies detected in the infrared K -band. This expands on a stacking analysis previously done in paper II. Finally in chapter 4 we discuss future outlook.

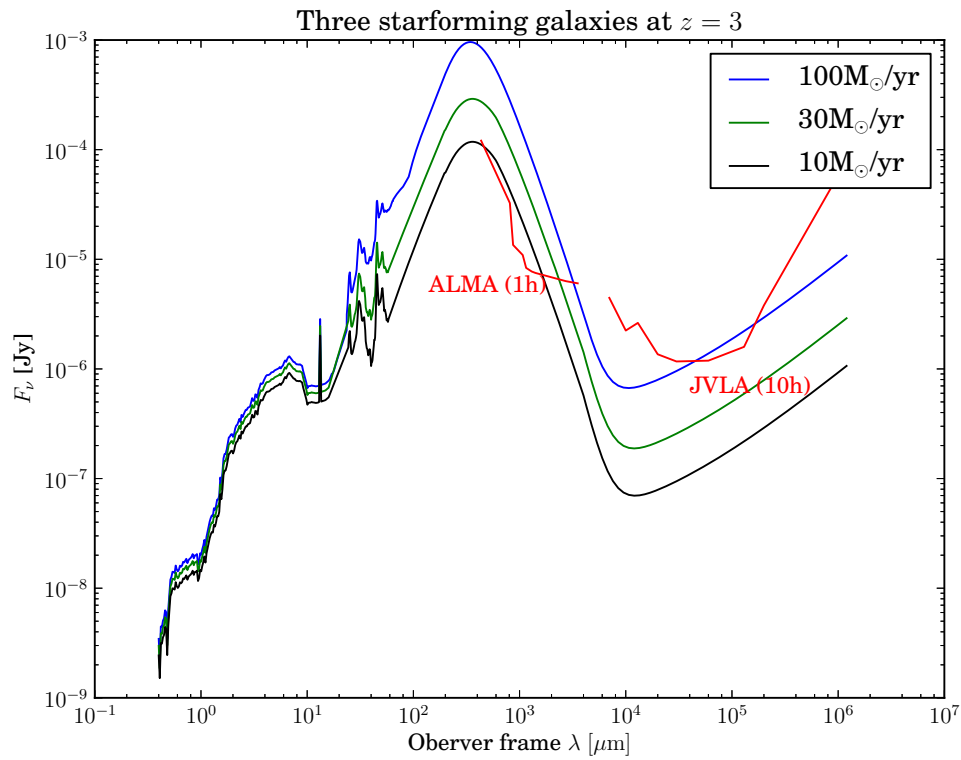


Figure 1.2: SED of three star-forming galaxies at $z = 3$. Red curves indicate sensitivity of full ALMA and JVLA. Note that in contrast to figure 1.1 we plot F_ν not νF_ν , however it is the same SED extended to longer wavelengths.

Stacking

Stacking is a statistical method to measure the average flux of sources that are too faint to be detected directly. It relies on *a priori* information on the location of the target sources. It works by averaging the emission from all target sources, and will result in a noise $\frac{\sigma}{\sqrt{N_{\text{stack}}}}$ where σ is the typical noise without stacking and N_{stack} is the number of target sources. Figure 2.1 illustrates a simple stacking procedure. A sample of sources is selected, i.e., a list of positions where we expect faint emission. For each position a 64×64 pixel stamp is cut out of the full image. All stamps are then averaged together on a pixel-by-pixel basis. This results in a stacked image with significantly lower noise than the individual stamps.

The technique of stacking is especially useful for studying the sub-mm and radio emission of high-redshift galaxies. Using the large photometric catalogues in from near ultraviolet to near infrared, such as MUSYC (Gawiser et al. 2006; Quadri et al. 2007; Cardamone et al. 2010) and the COSMOS catalogue (Capak et al. 2007), we can identify large samples of high-redshift galaxies. These galaxies can then be stacked in sub-mm and radio maps, which will allow us to study galaxies that would otherwise be out of reach of these telescopes.

For observations with single-dish telescopes at sub-mm and radio wavelengths the angular resolution is limited from around $20''$ at 345 GHz to around $10'$ at 1.4 GHz. This is significantly larger than the typical size of a high-redshift galaxy, which is typically less than $1''$ (e.g. Toft et al. 2007). This makes it difficult to ensure that the stacked emission originates in the target galaxies, and risks blending the emission from multiple galaxies in our beam. To avoid these issues we can use interferometric telescopes, such as ALMA and JVLA, which have much higher angular resolution. However, for interferometry, stacking is complicated by the fact that interferometry is not a direct imaging method. We are required to model the data to produce an image of the source. In paper I we investigate stacking of interferometric data, in particular for JVLA and ALMA.

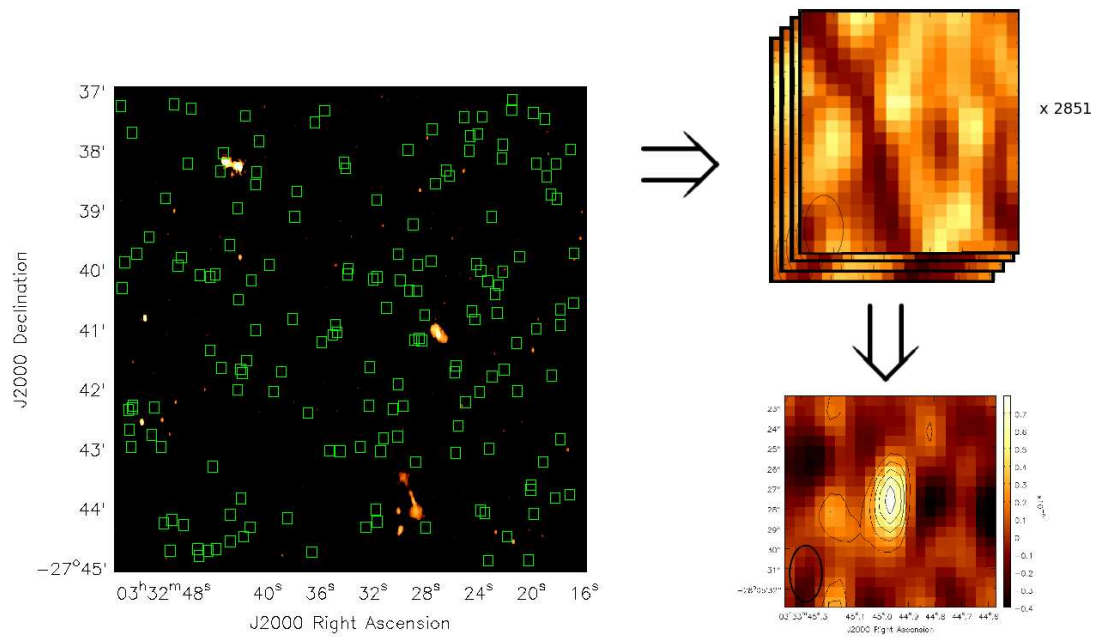


Figure 2.1: Illustration of stacking in the Extended Chandra deep field-south (ECDFS). In the example ~ 3000 Lyman-break galaxies are stacked in the Miller 1.4 GHz VLA map of the ECDFS (Miller et al. 2013). (Left) A $10' \times 10'$ segment of the 1.4 GHz VLA map. The stacking positions are marked in the map with green squares. (Top right) Map in a 16×16 pixel region around a typical stacking position, showing no detection. (Bottom left) Stacked image, showing 5σ detection.

We also propose a new method to perform stacking.

In this chapter I will first give an introduction to interferometry (section 2.1). In section 2.2 I expand on the discussion of the simulations used in the paper I. Finally in 2.3 I discuss the time and computer requirements of stacking.

2.1 Interferometry

Interferometry aims to simulate a large telescope by a collection of smaller telescopes. By using a technique known as *aperture synthesis*, we can produce an image with a typical resolution element of $1.22\lambda/D$, where D is the largest separation of dishes. This technique was originally developed by Martin Ryle and colleagues.

During observations each antenna records the incoming power over time to each antenna j as $P_j(t)$. A visibility is calculated between a pair of antennas j and k as

$$V_{j,k}(T) = \int_T^{T+dt} P_j(c)P_k(t)dt + i \cdot \int_T^{T+dt} P_i(c)P_j(t + 0.25/\nu)dt, \quad (2.1)$$

where i is the imaginary unit, T is the observation time, dt is the integration time, and ν is the frequency. This quantity is connected to the source we want to observe as

$$V_{j,k}(T) = \int_{\text{sky}} A_N(\vec{\sigma})I(\vec{\sigma})e^{-\frac{2\pi i}{\lambda}\vec{B}_{j,k}\cdot\vec{\sigma}}d\Omega, \quad (2.2)$$

where $\vec{\sigma}$ is a vector describing the position on the sky, $A_N(\vec{\sigma})$ is the primary beam attenuation, $I(\vec{\sigma})$ is the source brightness, and $\vec{B}_{j,k}$ is the separation of antenna j and k at the time T .

The position vector $\vec{\sigma}$ is generally expressed in terms of a local rectilinear coordinate system (l, m) where l is in the east direction and m is in the north direction, both in radians. The origin in this coordinate system is called the *phase centre*.

The primary beam attenuation depends on the antenna properties, such as size, location of the sub reflector, etc. In this work we assume that all antennas within the array are similar, as is true for JVLA and the ALMA main array. For telescopes with parabolic main reflector dishes, such as the JVLA and ALMA antennas, we can approximate the primary beam attenuation as

$$A(l, m) = e^{-\frac{2 \ln 2(l^2+m^2)}{(1.22\lambda/D_{\text{dish}})^2}}, \quad (2.3)$$

where D_{dish} is the antenna dish diameter and where it is assumed that the antennas are pointing towards the phase centre.

2.1.1 uv -coverage

The separation between antennas $\vec{B}_{j,k}$ is often expressed in terms of (u, v) which are defined such that $\vec{B}_{j,k} \cdot \vec{\sigma} = \lambda(ul + vm)$, i.e., (u, v) is the separation of the antennas in wavelengths as seen looking down from the phase centre. This simplifies equation 2.2 to

$$V(u, v) = \int_{\text{sky}} A_N(l, m) I(l, m) e^{2\pi i(ul+vm)} dl dm, \quad (2.4)$$

or the 2D Fourier transform of $A_N(l, m) I(l, m)$ evaluated at (u, v) . The 2D Fourier transform can be inverted to

$$I(l, m) = \frac{1}{A_N(l, m)} \int V(u, v) e^{-2\pi i(ul+vm)} du dv. \quad (2.5)$$

The plane spanned by (l, m) is referred to as the *image-plane* and the plane spanned by (u, v) is referred to as the *uv-plane*. We can only sample $V(u, v)$ where we have a pair of antennas with separation (u, v) . The points in the *uv-plane* where we have sampled $V(u, v)$ are referred to as the *uv-coverage*. Figure 2.2 illustrates the *uv-coverage* of the JVLA. In each integration we sample two points for each possible pair of antennas, i.e., in total, $N_{\text{antennas}}(N_{\text{antennas}} - 1)$ points are sampled where N_{antennas} is the number of antennas. As Earth rotates each pair traces out a track in the *uv-plane*, leading to greater *uv-coverage*.

As seen in figure 2.2 there is a “hole” in the middle of the *uv-plane* with no sampling. This “hole” is set by the closest antennas in the array. For sources with large spatial extent flux will be lost, since most of this will fall inside the “hole”. Similarly we cannot sample $V(u, v)$ outside the largest separation of antennas. This limits our resolution. However, for sources with small spatial extent, the full flux can still be sampled on shorter baselines. These effects can also be understood as a band-pass filter on the imaged data, where components with spatial scales outside the *uv-coverage* are filtered.

2.1.2 Imaging

The most common method used to produce $I(l, m)$ is the Fast Fourier Transform (FFT). This requires $V(u, v)$ to be sampled at regular intervals which the *uv-coverage* is not. To fix this *uv-gridding* is performed. This divides the *uv-plane* into a $N \times N$ grid. For each grid point the value is calculated from the visibilities that fall within the grid element. However, the uneven sampling of the *uv-plane* leads to very different number of visibilities in each grid point. Some grid positions contain no visibilities at all. From this we can define a sampling S , a $N \times N$ grid with the number of visibilities in each grid point. Running FFT

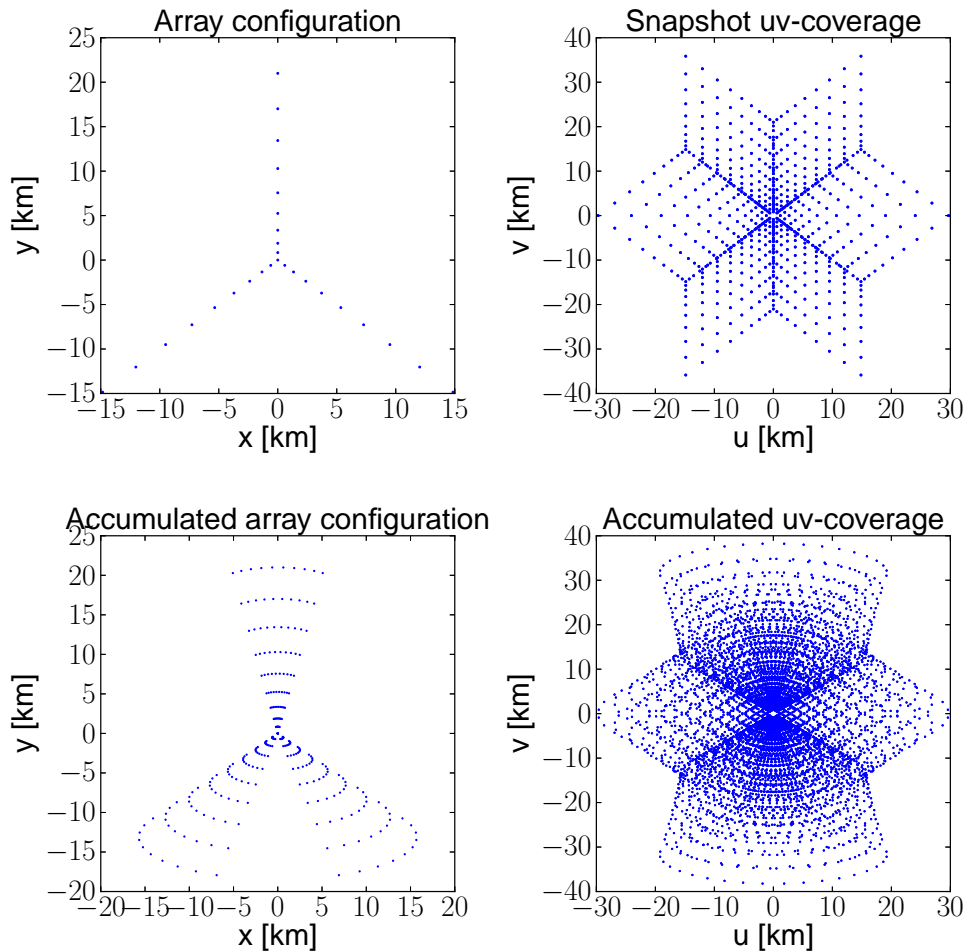


Figure 2.2: Illustration of array configuration and uv -coverage of JVLA. Observation at a declination of 10° with with a configuration similar to the JVLA A configuration. (top left) The JVLA array configuration as seen from the source. (top right) The corresponding uv -coverage to the JVLA array configuration. (bottom left) As the earth rotates, the array as seen from the source changes. The image shows how the array changes from 3 hours before the source passes the meridian until 3 hours after. (bottom right) We accumulate the snapshot uv -coverages to cover the uv -plane more fully.

on this grid results in the *dirty image* of $I(l, m)$, i.e., $I(l, m)$ convolved with the FFT of S .

The shape of S can be very uneven, and as such the resulting Fourier transform can contain strong peaks that are off from the main peak. This will introduce false sources in the dirty image and distort the shape of sources. To avoid this we can use a deconvolution algorithm, that attempts to remove the convolution. The most commonly used is CLEAN, Högbom (1974).

The limitation of any deconvolution algorithm is that there is no unique way to do this. There could be a number of different brightness distributions $I(l, m)$ that correspond to the same dirty image.

2.1.3 Wide field effects

For large field of view (FOV), we need to consider how the array appears for sources away from the phase centre. To do this properly, we need to describe the array in its full three dimensional configuration. This is done by adding a third coordinate w describing the separation of the telescopes along the line of sight. Equation 2.4 can then be expanded to

$$V(u, v, w) = \int_{\text{sky}} \frac{A_N(l, m)I(l, m)}{\sqrt{1 - l^2 - m^2}} e^{2\pi i(ul+vm+w(\sqrt{1-m^2-l^2}-1))} dl dm. \quad (2.6)$$

Equation 2.6 does not describe a 2D Fourier transform. We can not image this using the same method as equation 2.4. Instead we can use the *w-projection* algorithm. This grids the uv -plane for several different values of w and combines them into one image. This allows producing correct images for larger FOVs.

2.1.4 Translation and stacking

The Fourier transformation changes position information to frequency, and vice versa. This means that a source offset from the centre in the image-plane, will be centred in the uv -plane but multiplied by a complex plane wave. Accounting for the w term as well this can be described as

$$\xi_{(x_0, y_0)}(u, v, w) = e^{2\pi i(udx+vdw+w(\sqrt{1-dx^2-dy^2}-1))}. \quad (2.7)$$

where (dx, dy) is the vector pointing from the phase centre to (x_0, y_0) . If we want to recentre a source we can do this by multiplying $V(u, v, w)$ with the inverse of $\xi_{(x_0, y_0)}(u, v, w)$

$$\xi_{(x_0, y_0)}^{-1}(u, v, w) = e^{-2\pi i(udx+vdw+w(\sqrt{1-dx^2-dy^2}-1))}. \quad (2.8)$$

By using $\xi_{(x_0, y_0)}^{-1}(u, v, w)$ we can perform stacking in the uv -plane. For each target position we create a copy of the full uv -data, then we centre the position of interest by multiplying with $\xi_{(x_i, y_i)}^{-1}(u, v, w)$ where (x_i, y_i) are the coordinates of the stacking positions. After centring we can average the visibilities of each source to produce a new set of visibilities with an averaged (or stacked) version of our target sources.

Stacking by this method is limited by the fact that it does not allow to shift the (u, v, w) for different positions. This shift is a smaller effect than the phase correction $w(\sqrt{1 - dx^2 - dy^2} - 1)$. For the JVLA field of view of 30' at 1.4 GHz the shift in u and v will be typically less than a few per cent in each. Neither does the shift in (u, v, w) affect the total flux measured for our source, rather it changes the shape of the stacked source. This size error is close to the typical change in u and v , i.e., less than a few percent for JVLA at 1.4 GHz and significantly smaller for ALMA.

2.2 Simulation details, method of generation of sources.

Paper I uses simulated data to test the stacking algorithm. The simulated data are produced to mimic real data. This means that the data will not only contain the target sources, but also a population of other sources such that the full distribution of sources mimics what would be seen in a real observation. Due to noise on each visibility, it is impossible to fully deconvolve or remove the bright sources. Especially for JVLA, due to its large field of view that ensure many bright sources in each field of view. This means that the noise, even after deconvolution, will have a significant contribution from the side lobes of bright sources. As such, the flux distribution of the bright sources is important for the noise characteristics.

To produce data sets that mimics real data set we introduce two separate populations of sources into the data. We introduce one population of brighter sources, with the aim to achieve a good over all flux distribution. The second population we introduce is our target population. The target population consist of galaxies that are too faint to be individually detected and this population is used to evaluate our stacking algorithms.

In paper I we simulate 1.4 GHz JVLA observations and 230 GHz ALMA cycle 1 observations. All sources are generated as

$$I(x, y) = \frac{S_k}{\pi\sigma_k^2} e^{-\left(\frac{(x-x_k)^2 + (y-y_k)^2}{2\sigma_k^2}\right)}, \quad (2.9)$$

where S_k is the flux, (x_k, y_k) is the position, and σ_k is the size of source k . The sources are introduced directly in the uv -plane as

$$V(u, v, w) = S_k e^{-(u^2 + v^2)\pi^2\sigma_k^2} \xi_{(x_k, y_k)}(u, v, w) \quad (2.10)$$

When the size of the source approaches zero $I(x, y)$ approaches a two dimensional Dirac delta function $\delta(x - x_k, y - y_k)$. To avoid numerical imprecision when size is 0, $I(x, y)$ is replaced with $S_k \delta(x - x_k, y - y_k)$ and $V(u, v, w)$ with the corresponding uv -model $S_k \xi_{(x_k, y_k)}(u, v, w)$.

The coordinate (x_0, y_0) is generated uniformly in the field of view (FOV), i.e., $x_0 = x_c + U(-0.5, 0.5) \cdot \text{FOV}$ and $y_0 = y_c + U(-0.5, 0.5) \cdot \text{FOV}$ where (x_c, y_c) is the centre of the field and $U(\text{lower}, \text{upper})$ is a function that generates pseudo random numbers in the interval $[\text{lower}, \text{upper}]$ with a uniform distribution.

The field centre (x_c, y_c) is set to $(57.2957795^\circ, -30^\circ)$ for all simulations. The declination -30° was chosen to be similar to the declination of the Extended Chandra Deep Field-South (ECDFS). The right ascension was chosen at random as it does not impact on the data.

To generate the flux S_k we use flux distributions from observations of real sources. From the flux distribution we generate a cumulative distribution function F . This function is then modelled with a 2D spline to allow us to calculate the inverse function F^{-1} . The flux of our sources is then generated with $F^{-1}(U(0, 1))$. The exact form of F for our populations will be defined below.

2.2.1 Lyman-break galaxies

For JVLA we used a target population mimicking Lyman-break galaxies (LBGs). The luminosity function of LBGs is typically modelled in the rest frame ultraviolet by a Schechter function (Schechter 1976), e.g., Steidel et al. (1999); Bouwens et al. (2007). Note that this is the luminosity function and not the flux distribution. Doing this it is assumed that all LBGs are at similar distances.

The Schechter function is defined as

$$n(L/L_*) dL = \Phi^*(L/L_*)^\alpha e^{-L/L_*} dL, \quad (2.11)$$

where n is the differential number density of galaxies for a given luminosity, L_* is characteristic galaxy luminosity, and Φ^* is a normalisation for the overall space density. The free parameter α describes the low luminosity slope in a $\log n, \log S$ plot and a Schechter function with $\alpha = -1$ is called flat. Bouwens et al. (2007) measured α and L_* for LBGs from $z \sim 3$ to $z \sim 6$, they found values of $\alpha \approx -1.7$. It is important to note that at this α the number of low luminosity galaxies is infinite. As such it is only valid in a limited interval, and the distribution must be normalised in this interval.

The ultraviolet luminosity traces the star formation rate of the LBGs. Since radio continuum flux traces the same star formation we expect a similar luminosity function. Guided by this we generate target sources using a Schechter function with α and Φ^* as measured by Steidel et al. (1999). This results in a

cumulative distribution function

$$F(S) = \int_{0.1S_*}^S (x/S_*)^\alpha e^{-x/S_*} dx \Big/ \int_{0.1S_*}^{\infty} (x/S_*)^\alpha e^{-x/S_*} dx \quad (2.12)$$

where S is the flux and x is the integration variable for the differential flux distribution. We estimate S_* (flux distribution scaling, equivalent to L_*) from Carilli et al. (2008), where they estimate the flux from LBGs using stacking. To avoid divergence at low luminosity we generate no sources below $0.1L_*$, this is similar to the detection limit in Steidel et al. (1999). The parameter Φ^* is used to determine the number of sources to be generated in our field of view.

2.2.2 Radio flux distribution

The Schechter function only describes the flux of our faint star-forming galaxies. In a real map we will have a large number of bright sources, the distribution of these sources strongly impact the statistics in the map. As such it is important to not leave them out when we generate our simulated data sets.

In contrast to the faint star-forming galaxies, we can measure the flux of the bright sources directly. Bondi et al. (2008) examined the flux distribution of radio sources at 1.4 GHz in the COSMOS field. They fitted the flux distribution of sources down to 11 μ Jy, describing $\log n$ in terms a 6th order polynomial in $\log S$. Note that this describes the flux distribution rather than the luminosity function. Determining the luminosity function here would require to determine the redshift of our sources. This is not motivated in the context since only the flux distribution is of interest. As such we use the cumulative distribution function

$$F(S) = \int_{0.06 \text{ mJy}}^S x^{-2.5} 10^{\left[\sum_{q=0}^6 S_q \log_{10}(x)\right]} dx \Big/ \int_{0.06 \text{ mJy}}^{1 \text{ Jy}} x^{-2.5} 10^{\left[\sum_{q=0}^6 S_q \log_{10}(x)\right]} dx \quad (2.13)$$

where x is the integration variable for the differential flux distribution and S_q are the polynomial coefficients from Bondi et al. (2008).

2.2.3 Sub-mm flux distribution

At sub-mm wavelengths, most surveys are performed using single-dish telescopes with significantly lower resolution than ALMA. The distribution for ALMA may be different. Béthermin et al. (2012) studied the distribution of star-forming galaxies, to estimate flux distributions in ALMA bands. Hatsukade et al. (2013) observed with band 6 in ALMA cycle 0, and their results are consistent with the Béthermin et al. (2012) model. Therefore, we use the Béthermin

et al. (2012) flux distribution to generate data sets. The cumulative distribution function is generated numerically from galaxy count table.

We simulate mosaiced observations for ALMA, both contiguous and non-contiguous. The latter are motivated by surveys such as the ALESS survey by Hodge et al. (2013), a survey in which known bright sources in a field are targeted with ALMA. To simulate this we generate sources over a large field. The brightest sources are selected and the simulated data set has pointings centred at these. The fainter target sources are only generated inside these pointings.

2.3 Computational considerations

Our stacking algorithm requires that each visibility is read and recalculated once. There is no interdependence of visibilities, and as a result, time usage scales linearly with the number of visibilities. For each visibility we need to compute one complex exponential function for each position and frequency, and this would be the primary usage of processing power. Only positions that are visible in the pointing of the visibility affect the result, so that all other positions can be omitted. Assuming the computation is limited by the central processing unit (CPU), this results in a time usage that scales linearly in the number of positions in each pointing, as well as in number of channels per spectral window. We have evaluate code performance on a computer with an Intel Xeon E5-2620 with 6 physical cores through a test that stacks 100 positions (all visible in all pointings) with 26 million visibilities, 7 channels per spectral windows and 2 polarisations. This leads to an approximate CPU time estimate of

$$T_{\text{cpu}} = \frac{n_{\text{vis}} n_{\text{chan}} n_{\text{pol}} n_{\text{pos}} \cdot 96\text{ns}}{n_{\text{cpu}}}, \quad (2.14)$$

where n_{vis} is the number of visibilities, n_{chan} is the typical number of channels per spectral window, n_{pol} is the number of polarisations, n_{pos} is the typical number of positions per pointing, and n_{cpu} is the number of physical cores used.

In the case of a high performance CPU it is possible to be limited by disk read-write speed. Using double precision we arrive at a data rate of 9.8 MiB/s (one MiB being 2^{20} B). Significantly below the typical read-write speed of a 7200 rpm physical disk, but could pose an issue for a net mounted disk. The data rate decreases with a larger number of positions, since more CPU time is required per visibilities.

The requirement on physical random access memory (RAM) is low. We only need to cache sufficient data to avoid stuttering due to uneven disk read. Running with default parameters allocates ~ 0.5 MiB, which should not pose an issue on a modern computer.

The stacking software is built to operate within the frame-work of Common Astronomy Software Applications (CASA), McMullin et al. (2007). This allows

to perform other tasks required such as imaging of the stacked source. All such additional tasks will require more computer resources on top of those required by the stacking software.

Stacking of colour-selected galaxies with ALMA and VLA

Large surveys of high-redshift, dusty galaxies at sub-mm wavelengths have been carried out with single dish telescopes, such as James Clerk Maxwell Telescope (JCMT), the Atacama Pathfinder Experiment (APEX), and Herschel Space Telescope. One of the largest and deepest such surveys, is the LABOCA Extended Chandra Deep Field South Sub-mm Survey (LESS, Weiß et al. 2009). The LESS reached an RMS limit in flux density of 1.2 mJy over $30' \times 30'$, at an angular resolution of $19''.2$.

The ALESS (the ALMA survey of LESS-detected sources, Hodge et al. 2013; Karim et al. 2013) is a followup of the 126 sources detected in the LESS survey. These observations were carried out using ALMA in cycle 0 and have a typical resolution of $\sim 1''.6 \times 1''.15$ and sensitivity of 0.4 mJy/beam. The sensitivity of the ALESS is approximately 3 times deeper than the LESS. The tenfold improvement in angular resolution of ALMA ensures that sources are not blended and can be studied individually.

The work on paper II is led by Roberto Decarli. It reports the properties of four samples ($K_{\text{Vega}} < 20$, sBzK, ERO and DRG) by stacking in the ALESS data. My contribution primarily concerns the stacking of the ALESS data. I performed an independent image-stacking analysis of the ALESS data. I also proposed the algorithm of stacking random positions, used in paper II to estimate the uncertainty of the stacked result.

In this chapter I will expand on the stacking analysis of paper II with uv -stacking as developed in paper I. Section 3.1 and 3.2 describes additional data reduction steps required for stacking in the uv -domain. In section 3.3 the difference between uv - and image-stacking results is discussed. In section 3.4 we use the uv -stacking to study the sizes of the stacked populations.

3.1 Removing bright sources

The ALESS data contain a number of bright sources that are not part of our target populations. In paper I we found that the presence of such sources could negatively impact the results of stacking, especially in uv -stacking where such sources could not be cleaned after stacking. To avoid these issues all bright sources are modelled and removed if they are not part of the target population.

To do this we first image and clean all pointings individually. The cleaning uses an auto boxing algorithm where a box is added around each source brighter than 1.8 mJy. *Clean components*, i.e., model components corresponding to bright sources, are then only allowed from inside the boxes. From the model we remove all model components which are within 3 pixels from a stacking position. This avoids removing sources which are actually part of the target population. The resulting model of bright sources is then subtracted from the uv -data to produce a residual uv -data set.

3.2 Recalculating weights

The ALESS data set is a non-contiguous mosaic, with 122 pointings that do not overlap. When stacking in the uv -domain we need to combine visibilities from different pointings into one. This is done by concatenating the visibility from each pointing into a virtual pointing. Since the stacking procedure has moved the stacked sources into the phase-centre, this new combined image can be treated as a normal pointing.

However, studying the data we found that the sum of visibility weights of the different pointings varied greatly. This resulted in some pointings being mostly ignored in the stacked data set due to very low weights. Looking closer at the pointings with low visibility weights, we do not find the noise to be systematically higher than other pointings. To resolve some of these effects we recalculated the weights of the visibilities.

We did this by using the scatter of visibilities within each integration. For each integration we have 128 channels and 2 polarisations. This is a sufficiently large set of data points to estimate the σ for each integration, as the standard deviation of the 256 visibilities within each integration. The weights for the residual uv -data set were set to $1/\sigma^2$.

3.3 Results

Table 3.1 shows the results of uv - and image-stacking. The stacking samples are identical to the samples used in paper II. This means four different main samples: $K_{\text{Vega}} < 20$, sBzK, ERO and DRG. For exact definitions see paper II.

Apart from the full sample, we also stack four sub-samples for each sample. Three sub-samples exclude sources bright enough to be measured directly with no stacking, at flux limits of 3.6 mJy, 1.8 mJy, and 1.2 mJy. One sub sample is based on photometric redshift estimates and excludes all galaxies at $z < 1$.

The image-stacking results are taken from paper II with noise estimated as the standard deviation in an empty region of the stacked image. In image-stacking flux is estimated at the peak within a small search area around the centre in the stacked image.

To ensure uv -stacking is comparable we recentre the stacked source. For each stacked uv -data set we fitted a point source model to the data. The position of the fitted model (x_m, y_m) is then moved to the phase centre by multiplying each visibility with $\xi_{(x_m, y_m)}^{-1}(u, v, w)$. Model fitting is done using *uvmultifit* (Martí-Vidal et al. 2014). In uv -stacking, after centring, the flux is estimated as the weighted average of all visibilities using the visibility weights. Noise is calculated as one over the square root of the sum of visibility weights, which should estimate the typical noise of the visibilities since weights were calculated from the scatter of the visibilities.

For the full samples we also estimated the error by stacking random positions. Each stack is performed as follows:

1. Generate a set of random positions from the actual sample positions. Random positions are generated to be in the same pointings as the original sample positions. Within each pointing the positions are evenly distributed.
2. At each random position a source is introduced into the uv -data with the same flux as the average of the actual sample.
3. The random positions are stacked to produce a new stacked uv -data. The flux within this uv -data set is estimated as the weighted average of all visibilities using the visibility weights.

The random stack procedure is repeated 50 times for each sample. This results in a distribution of stacked fluxes. The errors are calculated as the sample standard deviation of this distribution.

The results indicate no large differences between uv - and image-stacking. This is consistent with what was found for stacking of non-contiguous ALMA mosaics in paper I. Looking at the results from the random stack, noise is similar in uv - and image-stacking. However, the noise estimate in uv -stacking from visibility weights (effectively visibility scatter) appears to underestimate noise by 30%-50%. We expect this to be similar for the sub-samples.

Table 3.1: Flux estimates with uv -stacking. Also for comparison shows image-stacking from Paper II. Error column is estimated by stacking fake sources introduced into the data .

Sample	N.gal	uv -stacking [mJy]	Error [mJy]	image-stacking [mJy]
All				
$K_{\text{Vega}} < 20$	100	0.81 ± 0.04	0.07	0.78 ± 0.06
sBzK	22	1.79 ± 0.09	0.12	1.88 ± 0.15
ERO	26	1.17 ± 0.08	0.12	1.11 ± 0.09
DRG	20	1.78 ± 0.10	0.13	1.77 ± 0.13
$S_{344\text{GHz}} < 3.6 \text{ mJy}$				
$K_{\text{Vega}} < 20$	97	0.54 ± 0.04	-	0.53 ± 0.06
sBzK	20	1.17 ± 0.09	-	1.31 ± 0.14
ERO	25	0.87 ± 0.09	-	0.82 ± 0.09
DRG	19	1.44 ± 0.08	-	1.41 ± 0.12
$S_{344\text{GHz}} < 1.8 \text{ mJy}$				
$K_{\text{Vega}} < 20$	90	0.26 ± 0.05	-	0.23 ± 0.05
sBzK	16	0.63 ± 0.11	-	0.77 ± 0.14
ERO	22	0.50 ± 0.09	-	0.45 ± 0.09
DRG	15	0.86 ± 0.09	-	0.89 ± 0.13
$S_{344\text{GHz}} < 1.2 \text{ mJy}$				
$K_{\text{Vega}} < 20$	85	0.13 ± 0.05	-	0.20 ± 0.06
sBzK	14	0.42 ± 0.12	-	0.60 ± 0.15
ERO	20	0.31 ± 0.10	-	0.39 ± 0.09
DRG	13	0.58 ± 0.09	-	0.68 ± 0.13
$z > 1$				
$K_{\text{Vega}} < 20$	52	1.17 ± 0.06	-	1.16 ± 0.09
sBzK	22	1.80 ± 0.09	-	1.89 ± 0.15
ERO	25	1.21 ± 0.09	-	1.15 ± 0.09
DRG	19	1.91 ± 0.08	-	1.90 ± 0.13

3.4 Sizes of stacked sources

3.4.1 Measurements

Both the image- and uv -stacking algorithms in section 3.3 assume that the target population is fully unresolved. With uv -stacking we are able to test this assumption since we have full uv -data for the stacked sources. If the target sources are point sources we expect the flux at long baselines to be the same as at short baselines. However, if the target sources are extended the flux will drop towards longer baselines. To test this we computed the flux for the stacked uv -data of our stacked full samples in three different bins in terms of baseline lengths. Within each bin the flux is calculated as the weighted average of all visibilities. Figure 3.1 shows the result, indicating that the stacked source is extended for each sample. We measure the size of this source using `uvmultifit` and fitting a Gaussian model to the stacked uv -data, see table 3.2. This results in a typical size of our sources of $\sim 1''$.

For comparison we also estimate the sizes of the same sample stacked at 1.4 GHz. The 1.4 GHz data are from the VLA survey by Miller et al. (2013) of the ECDFS. We use the uv -stacking method as for the ALMA data except for the weight calculations. The weights are calculated from the local noise around each stacking position, see paper I for detail description of the stacking procedure. The sizes at 1.4 GHz are similar to the sizes measured at 345 GHz.

The errors indicated next to the flux estimates in table 3.2 are calculated using the reduced chi square of our model fits. We also estimate the noise by stacking fake sources introduced into the data, similar to the method used for point sources. Instead of introducing point sources we introduce sources with the same Gaussian model found with `uvmultifit` on actual data. The flux and size is estimated by Gaussian fitting the stacked uv -data with `uvmultifit`, error calculated from the distribution of each.

3.4.2 Interpretation

There could be several possible reasons for the sizes seen in the stacked source. One limitation of stacking is the dependence on stacking positions. If the stacking positions are inaccurate it could cause the stacked source to appear extended, even if the actual target sources are compact. The cause of this could either be positional offsets between the near-infrared observations and the ALMA observations. Simpson et al. (2013) studied this for the brightest galaxies in the sample, and found the offsets to be smaller than $0''.3$. Such offsets would be of similar size and in similar direction for all sources in the data. This means that after the recentring this effect should be even smaller.

It is also possible that the near-infrared and the sub-mm emission do not originate from the same physical region in the target galaxies. Such offsets are

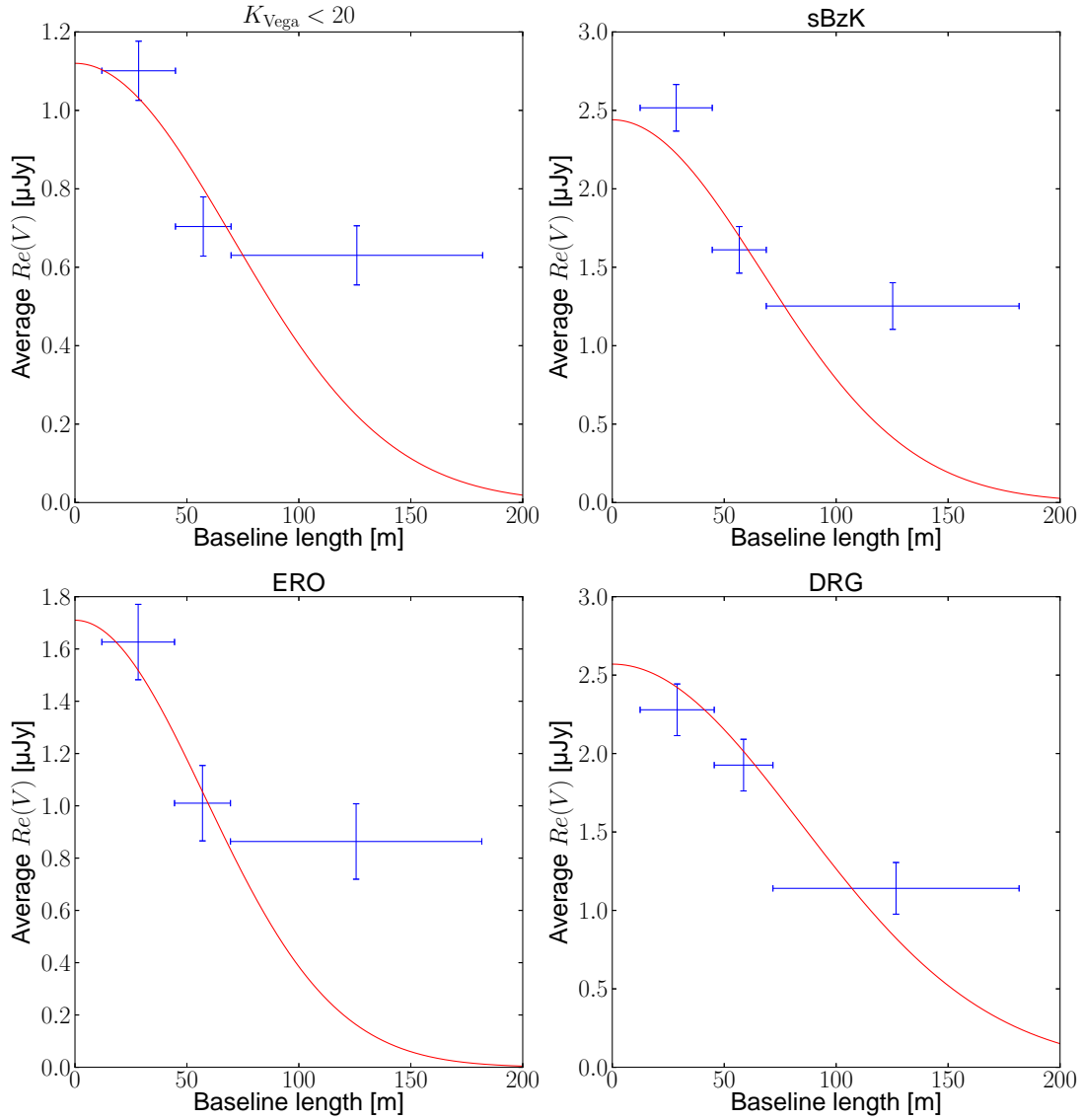


Figure 3.1: Stacked visibilities for each sample binned by baseline length. Each bin size is chosen to achieve similar noise in each bin. Red line indicates Gaussian uv -model fits to data using `uvmultifit`.

Table 3.2: Fluxes and sizes estimated using Gaussian model-fitting in `uvmultifit` for ALESS 345 GHz ALMA data and Miller 1.4 GHz VLA data. Error column indicates estimate of noise by stacking random sources introduced into the data.

Sample	N.gal	Flux	Flux error	Size	Size error
ALESS					
$K_{\text{Vega}} < 20$	100	1.12 ± 0.06 mJy	0.18 mJy	$0''.96 \pm 0''.08$	$0''.18$
sBzK	22	2.44 ± 0.13 mJy	0.52 mJy	$1''.02 \pm 0''.08$	$0''.22$
ERO	26	1.71 ± 0.15 mJy	0.29 mJy	$1''.16 \pm 0''.12$	$0''.34$
DRG	20	2.57 ± 0.14 mJy	0.38 mJy	$0''.80 \pm 0''.08$	$0''.18$
Miller VLA survey					
$K_{\text{Vega}} < 20$	100	22.2 ± 2.6 μ Jy	-	$0''.89 \pm 0''.20$	-
sBzK	22	37.8 ± 5.1 μ Jy	-	$1''.02 \pm 0''.22$	-
ERO	26	34.1 ± 5.0 μ Jy	-	$0''.91 \pm 0''.25$	-
DRG	20	35.3 ± 4.9 μ Jy	-	$0''.77 \pm 0''.25$	-

expected to be in random directions.

If we, however, interpret the measured sizes as the physical sizes of the target galaxies, this would indicate a physical size around 8 kpc. Toft et al. (2007) studied sizes of DRG in the near-infrared. They measured sizes at $1.6 \mu\text{m}$, which corresponds to a rest-frame wavelength close to V -band. At this wavelength light is dominated by light from stars, meaning that the size measured indicates the distribution of stars in the target galaxies.

They found some of the larger galaxies to have sizes close to 8kpc, but most were smaller. Our uv -stacked data are consistent with not all sources being extended, looking in figure 3.1 we can see an excess compared to a simple Gaussian model at the longer baselines. This would indicate that some of the target sources have smaller spatial extent and contribute additional flux at the longer baselines.

No matter the reason for the extension, it indicates that peak flux underestimates the flux from our population. Integrated values are typically 50 % larger than the values used in paper II. This would not change the general conclusions in the paper, the flux densities would be 3-5 greater than for field galaxies, rather than 2-3.

From the stacked sources we calculate average star-formation rates for the samples as well as the corresponding surface density, see table 3.3. For details on the calculations see section 1.2. For the sub-mm emission we use a dust temperature of T_{dust} of 30 K and β of 1.6, based on stacking of Herschel data in paper II.

Hodge et al. (2013) studied the bright sub-millimeter galaxies in the ALESS data and found a median lower limit on the star formation rate surface den-

Table 3.3: Star formation rates for each sample using stacked sub-mm and 1.4GHz flux.

Sample	$\langle z \rangle$	SFR_{FIR} $M_{\odot} \text{ yr}^{-1}$	$\text{SFR}_{1.4\text{GHz}}$ $M_{\odot} \text{ yr}^{-1}$	$\Sigma_{\text{SFR}}(\text{FIR})$ $M_{\odot} \text{ yr}^{-1} \text{ kpc}^{-2}$	$\Sigma_{\text{SFR}}(1.4\text{GHz})$ $M_{\odot} \text{ yr}^{-1} \text{ kpc}^{-2}$
$K_{\text{Vega}} < 20$	1.562	61	76	1.79	1.90
sBzK	1.896	137	202	3.10	4.56
ERO	1.502	93	106	2.60	1.82
DRG	1.792	143	165	5.64	6.03

sity of $14 M_{\odot} \text{ yr}^{-1} \text{ kpc}^{-2}$. Our samples all fall below this, with the sBzK and $K_{\text{Vega}} < 20$ samples falling within the range of the “normal” local universe spiral galaxies studied by Kennicutt (1998). Our sBzK results are also consistent with results from Daddi et al. (2010), who found star formation rate surface densities around $1 M_{\odot} \text{ yr}^{-1} \text{ kpc}^{-2}$ for BzK galaxies. Daddi et al. (2010) used ultraviolet and CO emission to estimate the size of the star-forming region. The DRG sample appears to have slightly higher surface densities, with values typically found in luminous infrared galaxies (LIRGs) in the local universe, such as the galaxies in GOALS survey (Armus et al. 2009).

Outlook

The stacking algorithms described in this work are for continuum emission. However, if we have redshifts for our target galaxies we can also search for line emission. One aim is to extend the uv -stacking algorithm in paper I to work for line stacking by shifting the frequency channels for each galaxy. This would allow to study lines such as the CO rotational lines to determine the gas reservoir properties high redshift galaxies.

The stacking size measurements in section 3.4 show great promise to study the sizes of very faint galaxies. Applying this technique to deep maps with higher angular resolution would be natural. For example, e-MERLIN will achieve an angular resolution of $0''.2$ at 1.4 GHz. With the legacy survey e-MERGE (e-MERlin Galaxy Evolution Survey), the e-MERLIN will survey high redshift galaxies and AGN at a few GHz. Using uv -stacking we will be able to study both sizes and fluxes of faint high redshift galaxies out of range of direct detection.

The size analysis of section 3.4 is carried out for sources with sizes close to that of the restoring beam. However, studying emission from significantly larger structures is of scientific interest. Clusters are associated with faint, diffuse radio halos. Detecting this emission is challenging as the large part of the emission falls on the shortest baselines, which has been found to be problematic for VLA maps, see paper I. By using uv -stacking, it will be possible to analyse the post-stacking trends on short baselines. This will be important to reliably stack emission from very extended radio sources.

The Square Kilometre Array (SKA) is planned to be able to survey the radio sky at unprecedented speeds. This will provide many opportunities for stacking, to study previously unstudied populations of galaxies. With this in mind, our uv -stacking algorithm is designed to be highly scalable and is fully parallelised. As such, it will run efficiently on either CPU-clusters or high-throughput clusters equipped with graphical processing units (GPUs). This

will allow us to work with the large SKA data sizes. While still slower than image-stacking, *uv*-stacking provides a number of advantages. For example, compared to JVLA, SKA will be observing with even higher dynamic range. As seen in paper I, high dynamic range does provide additional challenges in stacking. But with *uv*-stacking we are able to alleviate this effect.

Bibliography

- Armus, L., Mazzarella, J. M., Evans, A. S., et al. 2009, *PASP*, 121, 559
- Beelen, A., Cox, P., Benford, D. J., et al. 2006, *ApJ*, 642, 694
- Béthermin, M., Daddi, E., Magdis, G., et al. 2012, *ApJ*, 757, L23
- Bondi, M., Ciliegi, P., Schinnerer, E., et al. 2008, *ApJ*, 681, 1129
- Bouwens, R. J., Illingworth, G. D., Franx, M., & Ford, H. 2007, *ApJ*, 670, 928
- Bouwens, R. J., Illingworth, G. D., Oesch, P. A., et al. 2011, *ApJ*, 737, 90
- Capak, P., Aussel, H., Ajiki, M., et al. 2007, *ApJS*, 172, 99
- Cardamone, C. N., van Dokkum, P. G., Urry, C. M., et al. 2010, *ApJS*, 189, 270
- Carilli, C. L., Lee, N., Capak, P., et al. 2008, *ApJ*, 689, 883
- Chabrier, G. 2003, *PASP*, 115, 763
- Chary, R. & Elbaz, D. 2001, *ApJ*, 556, 562
- Condon, J. J. 1992, *ARA&A*, 30, 575
- Daddi, E., Bournaud, F., Walter, F., et al. 2010, *ApJ*, 713, 686
- Daddi, E., Cimatti, A., Renzini, A., et al. 2004, *ApJ*, 617, 746
- Ellis, R. S., McLure, R. J., Dunlop, J. S., et al. 2013, *ApJ*, 763, L7
- Elston, R., Rieke, G. H., & Rieke, M. J. 1988, *ApJ*, 331, L77
- Finkelstein, S. L., Papovich, C., Dickinson, M., et al. 2013, *Nature*, 502, 524
- Franx, M., Labbé, I., Rudnick, G., et al. 2003, *ApJ*, 587, L79

- Gawiser, E., van Dokkum, P. G., Herrera, D., et al. 2006, *ApJS*, 162, 1
- Hatsukade, B., Ohta, K., Seko, A., Yabe, K., & Akiyama, M. 2013, *ApJ*, 769, L27
- Hodge, J. A., Karim, A., Smail, I., et al. 2013, *ApJ*, 768, 91
- Högbom, J. A. 1974, *A&AS*, 15, 417
- Karim, A., Swinbank, A. M., Hodge, J. A., et al. 2013, *MNRAS*, 432, 2
- Kennicutt, Jr., R. C. 1998, *ApJ*, 498, 541
- Leitherer, C. & Heckman, T. M. 1995, *ApJS*, 96, 9
- Martí-Vidal, I., Vlemmings, W. H. T., Muller, S., & Casey, S. 2014, accepted for publication in *A&A* (arXiv: 1401.4984)
- McMullin, J. P., Waters, B., Schiebel, D., Young, W., & Golap, K. 2007, in *Astronomical Society of the Pacific Conference Series*, Vol. 376, *Astronomical Data Analysis Software and Systems XVI*, ed. R. A. Shaw, F. Hill, & D. J. Bell, 127
- Miller, N. A., Bonzini, M., Fomalont, E. B., et al. 2013, *ApJS*, 205, 13
- Oesch, P. A., Bouwens, R. J., Illingworth, G. D., et al. 2013, *ApJ*, submitted (arXiv: 1309.2280)
- Planck Collaboration, Ade, P. A. R., Aghanim, N., et al. 2013, *A&A*, submitted (arXiv: 1303.5076)
- Quadri, R., Marchesini, D., van Dokkum, P., et al. 2007, *AJ*, 134, 1103
- Schechter, P. 1976, *ApJ*, 203, 297
- Simpson, J., Swinbank, M., Smail, I., et al. 2013, *ApJ*, submitted (arXiv: 1310.6363)
- Steidel, C. C., Adelberger, K. L., Giavalisco, M., Dickinson, M., & Pettini, M. 1999, *ApJ*, 519, 1
- Steidel, C. C., Pettini, M., & Hamilton, D. 1995, *AJ*, 110, 2519
- Toft, S., van Dokkum, P., Franx, M., et al. 2007, *ApJ*, 671, 285
- Weiß, A., Kovács, A., Coppin, K., et al. 2009, *ApJ*, 707, 1201

Paper I

Stacking of large interferometric data sets in the image- and uv-domain – a comparative study

L. Lindroos, K. K. Knudsen, W. Vlemmings, J. Conway, and I. Martí-Vidal

Submitted to Monthly Notices of the Royal Astronomical Society

Paper II

An ALMA Survey of Sub-millimeter Galaxies in the Extended Chandra Deep Field South: Sub-millimeter Properties of Color-selected Galaxies

R. Decarli, I. Smail, F. Walter, A. M. Swinbank, T. R. Greve, J. A. Hodge, R. Ivison, A. Karim, K. K. Knudsen, L. Lindroos, H. W. Rix, E. Schinnerer, J. M. Simpson, P. van der Werf, and A. Weiß

ApJ, Vol. 780, pp. 115-127, 2014